

Article

Polarization Coupling between Ferroelectric Liquids and Ferroelectric Solids: Effects of the Fringing Field Profile

Stefano Marni ¹, Raouf Barboza ¹, Ayomide S. Oluwajoba ¹, Riccardo Zamboni ^{2,3} and Liana Lucchetti ^{1,*}

¹ Dipartimento SIMAU, Università Politecnica delle Marche, Via Brecce Bianche, 60131 Ancona, Italy; s.marni@univpm.it (S.M.); r.barboza@univpm.it (R.B.); s1101521@studenti.univpm.it (A.S.O.)

² Institute of Applied Physics, University of Münster, Correnstr. 2/4, 48149 Münster, Germany; riccardo.zamboni@uni-muenster.de

³ Dipartimento di Fisica e Astronomia G. Galilei, Università di Padova, 35131 Padova, Italy

* Correspondence: l.lucchetti@univpm.it

Abstract: Recent experiments devoted to characterizing the behavior of sessile ferroelectric liquid droplets on ferroelectric solid substrates have shown the existence of a droplet electromechanical Rayleigh-like instability. The instability is induced by the bulk polarization of the ferroelectric fluid, which couples to the polarization of the underlying substrate through its fringing field and solid–fluid interface coupling. With the aim of characterizing this phenomenon, namely the coupling between the polarizations of a fluid and a solid material, we studied the behavior of ferroelectric liquid droplets confined between two solid substrates, arranged in different configurations, realized to generate fringing fields with different profiles. The results show that the features of the droplets instability are indeed affected by the specific fringing field shape in a way dominated by the minimization of the electrostatic energy associated with the bulk polarization of the ferroelectric fluid.

Keywords: ferroelectric nematic liquid crystals; lithium niobate; fringing field; polarization coupling



Citation: Marni, S.; Barboza, R.; Oluwajoba, A.S.; Zamboni, R.; Lucchetti, L. Polarization Coupling between Ferroelectric Liquids and Ferroelectric Solids: Effects of the Fringing Field Profile. *Crystals* **2024**, *14*, 425. <https://doi.org/10.3390/crust14050425>

Academic Editor: Ingo Dierking

Received: 10 April 2024

Revised: 25 April 2024

Accepted: 27 April 2024

Published: 29 April 2024



Copyright: © 2024 by the authors. Licensee MDPI, Basel, Switzerland. This article is an open access article distributed under the terms and conditions of the Creative Commons Attribution (CC BY) license (<https://creativecommons.org/licenses/by/4.0/>).

1. Introduction

The discovery of the ferroelectric nematic phase [1–5] was a groundbreaking event, since the combination of fluidity in ferroelectric fluid and its polar coupling to electric fields allow the observation of a whole new world of phenomena, which are rapidly becoming the focus of an increasing number of scientists, as demonstrated by the large number of peer review articles already published on the subject [6–16].

In this scenario, we recently performed experiments aimed at characterizing the behavior of sessile ferroelectric nematic liquid crystal droplets into contact with a ferroelectric solid substrate [8]. We observed that upon entering the ferroelectric nematic phase, droplets experience an electromechanical instability that manifests itself through the sudden ejection of fluid jets, which branch into smaller streams and eventually form secondary tiny droplets [8]. This behavior resembles the instability predicted by Lord Rayleigh in 1882, for charged conductive liquid droplets that are above the critical charge-to-volume ratio [17]. Since ferroelectric nematic droplets are neutral, in our case this process occurs in the absence of free charges, but the required charging within the droplet arises from the intrinsic polarization of the ferroelectric liquid crystal via its contact with the ferroelectric substrate. The coupling between the polarization in the solid and fluid materials is mediated by the fringing field generated by the pyroelectric charging of the substrate. This polarization coupling induces the accumulation of surface charges on the droplet–air interface. As the droplet polarization grows by cooling the material, the local accumulation of polarization charges produces repulsive forces that overcome the surface tension. As this condition is met, the instability turns to an explosive runaway process, since the flow of the ferroelectric liquid crystal in the arising jet induces the orientational order of the nematic director along

the jet direction. This transports polarization charge to the tip, thereby increasing the electrostatic repulsion.

The observed polarization-induced droplet instability crucially depends on the properties of the ferroelectric nematic phase and on the combination of polarization and fluidity unique to this system. Ferroelectric nematic liquid crystals offer for the first time the opportunity of studying the coupling between the polarization of a fluid and a solid ferroelectric, which understanding might provide the basis for novel electro-hydromechanical applications.

In this work, we aim at characterizing in detail the effects of the fringing field created by the ferroelectric substrate on the droplets' instability. To this purpose, we did not work with sessile droplets but confined them between two ferroelectric substrates arranged in two different ways, to generate fringing fields with different profiles. Specifically, we realized sandwich cells where the substrates' polarization vectors are parallel or antiparallel to each other, so to develop opposite or equal surface electrostatic charges at the interfaces with the liquid crystal droplet.

Noteworthy, conventional nematic liquid crystals in combination with ferroelectric substrates have been studied in several different configurations see for example [18,19]. The consequence of substrate charging on the liquid crystal's average molecular orientation has been demonstrated; however, no effect comparable to those observed with ferroelectric nematic droplets has been reported.

2. Materials and Methods

The ferroelectric liquid crystal used in this work is 4-[(4-nitrophenoxy)carbonyl]phenyl 2,4-dimethoxybenzoate (RM734). This compound was synthesized as described in [1], and its structure and phase diagram have already been reported [1]. The ferroelectric nematic phase (N_F) appears here through a weakly first order phase transition upon cooling from the conventional higher temperature nematic (N) phase and is stable in the temperature range 133–80 °C [1]. The value of the spontaneous polarization P of RM734 exceeds 6 $\mu\text{C}/\text{cm}^2$ at the lowest temperature in the N_F phase; moreover, P is locally collinear to the molecular director \mathbf{n} , defining the average orientation of the molecular axis, and is either parallel or antiparallel to it [1].

As ferroelectric solid substrates, we used 900 μm thick z-cut undoped lithium niobate (LN) crystals (PI-Kem). Although the bulk spontaneous polarization of LN crystals along the [0001] z-axis is of the order of 70 $\mu\text{C}/\text{cm}^2$, because of very efficient compensation mechanisms at the z-cut surfaces, the surface charge at equilibrium is only of the order of about $10^{-2} \mu\text{C}/\text{cm}^2$ [20]. When, however, temperature variations are induced in the crystal, the surface charge of LN can significantly increase thanks to the pyroelectric effect [21–23], a transient phenomenon observable during and shortly after the temperature variation, and due to the slow free charge relaxation in LN. The pyroelectric coefficient of undoped LN is known to be of the order of $10^{-4} \text{ C}/\text{m}^2\text{K}$ at room temperature [24], increases by one order of magnitude around 100 °C [25]. Given the temperature used in our experiments, dictated by the RM734 phase diagram, we can thus expect an induced surface charge density of the order of 1 $\mu\text{C}/\text{cm}^2$, for temperature variations of a few degrees, ramped in a short time compared to the LN charge relaxation. To match the conditions of the previous work on sessile droplets [8], LN crystals were used as bare substrates, with no coating applied.

To prepare the samples used in this work, a RM734 droplet was deposited on a LN substrate at a temperature $T = 200$ °C, which corresponds to the liquid crystal isotropic phase, and then covered by a second LN slab, previously heated at the same T. RM734 droplets were realized following two steps. First, a small amount of RM734 powder was deposited at room temperature on a clean glass slide and heated to 150 °C until it melted. To create the initial droplets, a cold stainless needle was dipped into the melt and retracted, causing the droplet on its tip to solidify upon contact with the surrounding air. To increase the size of the RM734 “pearl”, rapid (to avoid re-melting) successive dipping is performed. Then, the pearl was remelted into a droplet on the heated LN substrate. The two substrates

were then stuck together by means of two 100 μm thick stripes of Kapton tape, which also define the cell thickness. The liquid crystal droplet confined between two solid substrates assumes the form of a capillary bridge (Figure 1a). The entire cell was then transferred to a small, closed oven, suitable for the optical microscope, and cooled down to the N_F phase. In order to perform a systematic analysis of the instability events, we decreased the cell temperature by steps of 5 °C ramped in 60 s each, resulting in a cooling rate of 0.08 °C/s. Due to the structure of the oven used, the temperature variation is the same in the entire cell, which guarantees the same amount of pyroelectric charging on both the LN confining crystals.

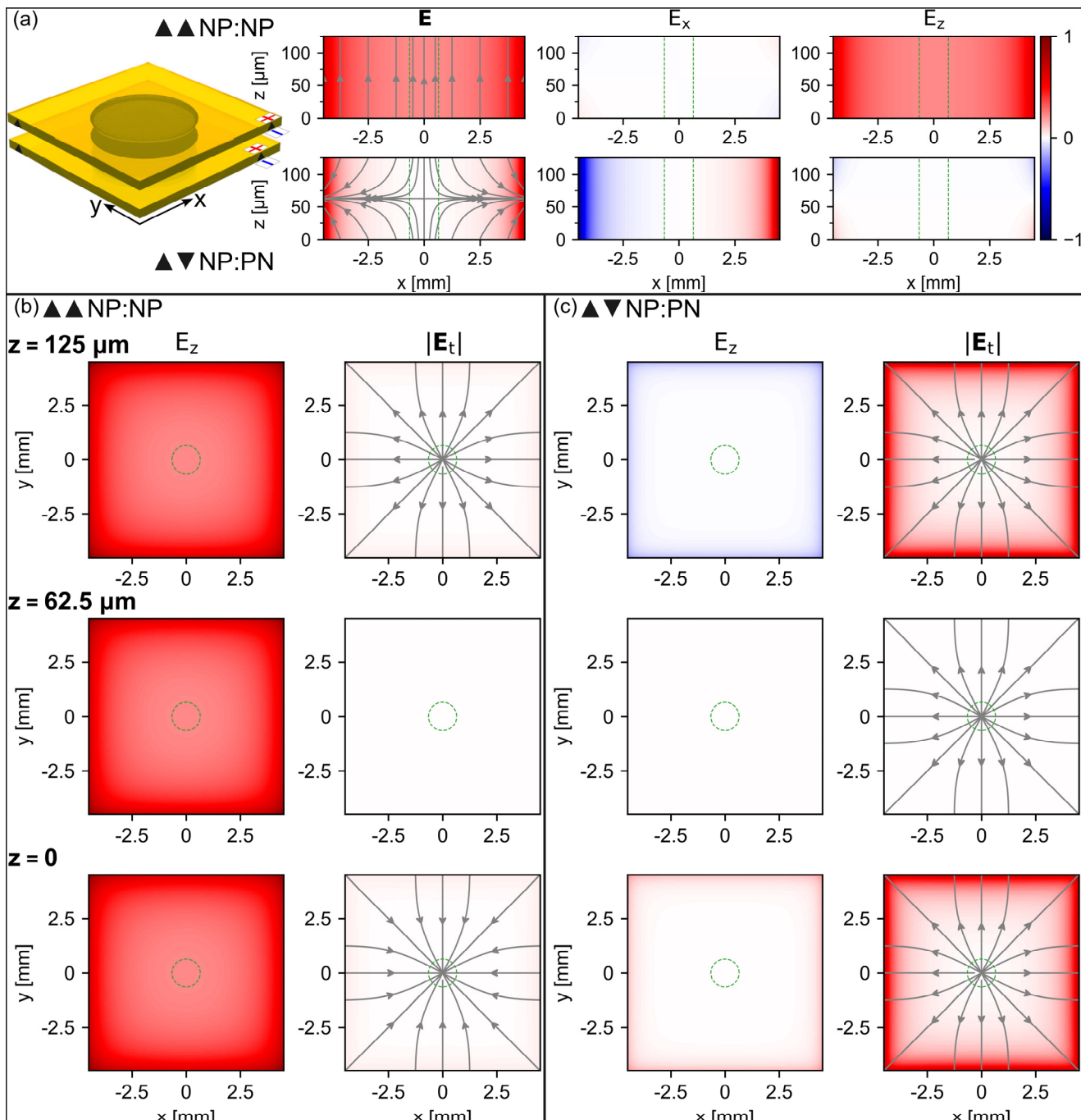


Figure 1. Sketch of the liquid crystal cells used in this work and fringing field profile and value in the two configurations. (a) The left-hand side shows the sketch of an RM734 droplet confined between two LN slabs, assuming the form of a capillary bridge. The two LN substrates in the sketch have

parallel polarization vectors and develop opposite charges at the interface with the liquid crystal, which corresponds to the *np/np* configuration. Right-hand side reports the normalized fringing field with its z and x-components at $y = 0$. The top line refers to *np/np*, the bottom line to *np/pn*. **(b)** Vertical (E_z) and in-plane (E_t) components of the fringing field at different positions along the cell thickness d , for the *np/pn* configuration. **(c)** Same as panel b, for the *np/np* configuration. The maximum values of the fringing field are $|E_{\text{ff}}|_{\text{max}} = 843 \text{ V/cm}$ for *np/np* and $|E_{\text{ff}}|_{\text{max}} = 321 \text{ V/cm}$ for *np/pn*.

The liquid crystal cells realized with two LN substrates are of two different kinds. Specifically, LN crystals were arranged so as to expose equally or oppositely charged surfaces at the interfaces with the liquid crystal, as sketched in Figure 1a. The two configurations will be referred to as *np/pn* and *np/np*, where *n* and *p* stand for negative and positive, respectively. Noteworthy, the large thickness of the cells (100 μm) makes the droplets' volume high enough to balance the additional friction due to confinement and the much lower thermal gradients on the LN substrates resulting from the closed arrangement.

The details of the electromechanical droplets' instability have been analyzed by POM observations and videos recorded by a CCD camera operating at 25 frames per second.

3. Results and Discussion

Due to the finite size of LN crystals, their pyroelectric charging gives rise to an external fringing field. This field is a fraction f of the internal field $\sigma_{\text{LN}}/\epsilon_0$, with f depending on the crystal shape and size, and of the order of $f \approx 10^{-3}$ in our experimental conditions [8]. The fringing fields generated by the LN slabs combine in different ways in *np/np* and *np/pn* cells, which results in different profiles and values of the total field present within the region between the substrates. The total fringing field E_{ff} in the two cells, in the absence of the liquid crystalline fluid bridge, is reported in Figure 1. Figure 1a shows the normalized field E (intensity and lines) and its x- and z-components on the xz plane at $y = 0$ for the two configurations (top: *np/np*; bottom: *np/pn*). The *np/pn* arrangement gives rise to a total fringing field, which is mainly vertical and quite uniform along the cell thickness. The x-component is different from zero, although very weak, only close to the substrate's corners. On the contrary, the *np/np* configuration produces a total fringing field with a very weak vertical component, different from zero only at the corners, and an x-component that is uniform along the thickness, and increases from the center to the edges of the LN plates. The vertical and in-plane field components are reported in panels b (*np/np*) and c (*np/pn*) at three different positions along the cell thickness d : $z = 0$, $z = d/2$ and $z = d$. For the in-plane component E_t , the field lines are also shown. They are radially distributed on the xy planes. The absolute values of the field are also different in the two cells, being about $8.4 \times 10^5 \text{ V/m}$ for the *np/np* cells and $3.2 \times 10^5 \text{ V/m}$ for the *np/pn* ones (maximum values).

The specific profile of E_{ff} affects the features of the electromechanical instability of the N_F fluid bridge. In particular, (i) the number of instability events observed within the temperature window corresponding to the N_F phase, (ii) the number of ejected fluid jets for each of these events and (iii) the temperature at which these events start, depend on the specific substrates' arrangement. This is shown in Figure 2a, where the number N of observed fluid jets is reported as a function of the instability temperature T_i , defined as the temperature at which the instability event takes place. Different colors correspond to different kinds of cells. It is evident that the instability starts at higher temperatures in *np/np* cells, which thus exhibit the highest number of instability events. Moreover, these events are, on average, characterized by the highest number of ejected jets. Since a higher temperature corresponds to a lower value of the N_F polarization P [1], the results in Figure 2a indicate that in *np/np* cells, the charging threshold is reached for lower values of P than in the other kind of cells.

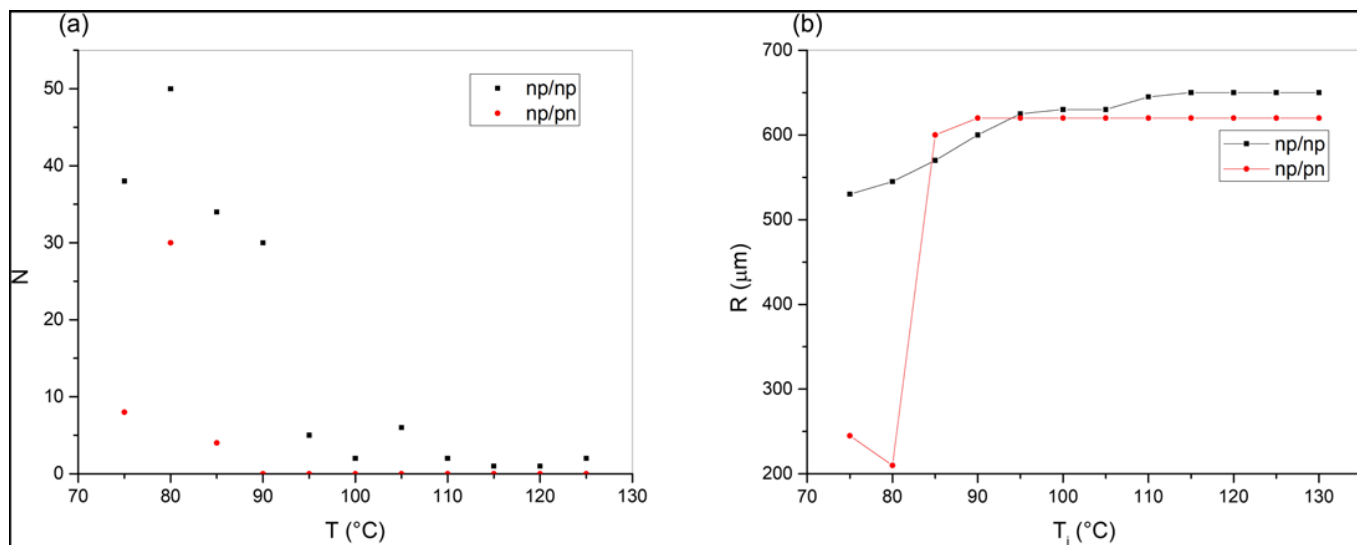


Figure 2. (a) Number of fluid jets ejected for each instability event for *np/np* (black squares) and *np/pn* (red circles) cells, as a function of the instability temperature T_i ; (b) average radius of the N_F fluid bridge measured from the cells' top view, after each instability event for *np/np* (black squares) and *np/pn* (red circles) cells, as a function of the instability temperature T_i . Full lines are just guides for the eyes. Data shown in the figure are related to two specific cells. However, the same measurements have been repeated several times on different samples and gave similar results.

The *np/np* configuration, with its mainly vertical and uniform fringing field, is similar to the geometry used by Mathe et al. in [26]. In their study, a ferroelectric fluid bridge was confined between two conductive glasses and an external electric field was applied perpendicular to the cell substrates. The instability caused by this field was interpreted as a kind of labyrinthine instability, already observed both in magnetic fluid exposed to a magnetic field orthogonal to the bounding plates and in dielectric fluids [27–29]. In both cases, the presence of a gap separating the fluid from the magnetic poles or from the electrodes is necessary for the instability to take place. Such a gap allows the presence of a field component parallel to the plates. In our case, the gap is intrinsically present since LN is itself an insulator.

The presence of the ferroelectric fluid bridge changes the fringing field profile reported in Figure 1. In *np/np* cells, this change consists in the appearance of an additional component of the field parallel to the bounding surfaces. It is known that the bulk polarization of the N_F liquid crystal spontaneously self organizes to minimize the internal and external electric fields. Generally, \mathbf{P} will end up parallel to the interfaces to avoid the accumulation of surface charge $\sigma = \mathbf{P} \cdot \mathbf{u}$ (where \mathbf{u} is the unit vector perpendicular to the surfaces). Additionally, \mathbf{P} will adopt bend deformations, which do not produce space charge, thus preventing nonzero $\nabla \cdot \mathbf{P}$ as much as compatible with geometric constraints. In the presence of the fringing field, which in this geometry is mainly normal to the LN/ N_F interface planes, the ferroelectric nematic becomes polarized. This happens through a small reorientation of \mathbf{P} by an angle such that it deposits polarization charge on the fluid bridge surfaces, canceling the internal field, a peculiarity of the N_F phase referred to as “fluid superscreening” [8,13]. This process leads to a mismatch between the field inside the bridge and the one outside. Indeed, in the first case, the potential difference is virtually negligible, being due to the field in the thin gap between the LN-charged surface and the liquid crystal interfacial layer; in the second case, the potential difference is determined by the field in air. This mismatch generates an additional in-plane component of the field, which can be arbitrarily large, depending on the thickness of the layer along which the potential difference changes from zero to the value $d\sigma_{LN}/\epsilon_0$. The additional field component drives jet ejection from the charge accumulation sites. The result is the occurrence of several

instability events, characterized by the ejection of a large number of jets from different portions of the capillary bridge at the interfaces with the bounding plates (Figure 3a–d).

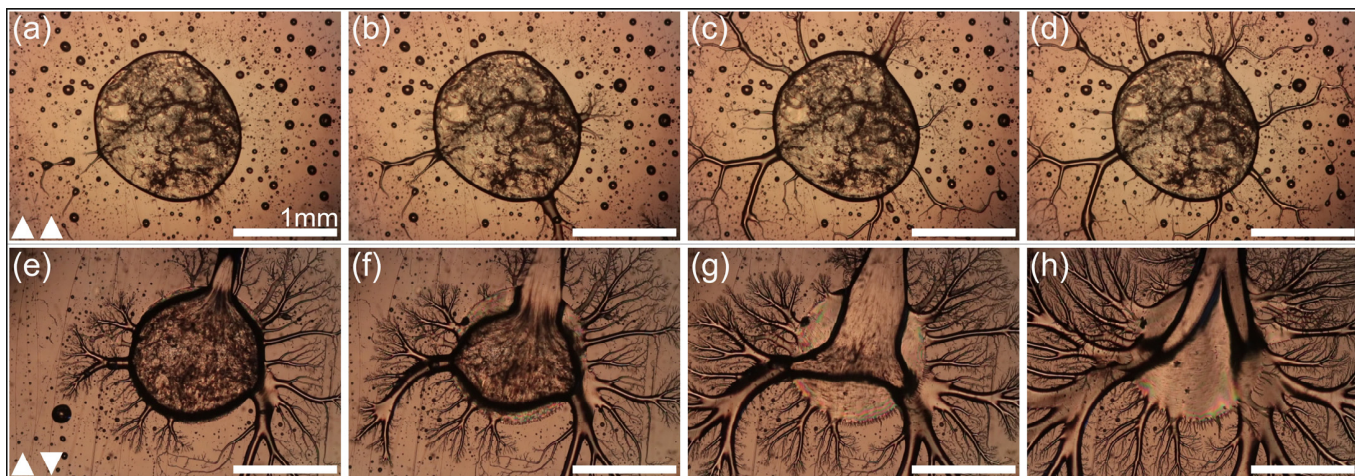


Figure 3. Examples of the observed electromechanical instability in N_F fluid bridges formed by confining an RM734 droplet between two LN crystals. (a,d) Sequence of frames showing the evolution of the instability in the np/np configuration. The onset of instability consists in the formation of several small spikes protruding from different regions of the bridge rim (a). As the instability proceeds, some jets grow (b) and new ones appear (c,d). Some of the jets are clearly ejected from locations on different planes, namely the two LN/N_F interface planes. (e,h) Sequence of frames showing the evolution of the instability in the np/pn configuration. In this case, jets rapidly grow in diameter (e,f), encompassing large portions of the droplet rim and volume on both interface planes (g,h). Note that the small droplets already present in the images (a,e) are due to fragmentation of the main droplet during sample preparation. Frames are not consecutive.

An additional feature of np/np cells is the temperature at which the instability starts, which is higher than that in np/pn cells, a behavior that we ascribe to the higher value of E_{ff} components that characterize this specific substrates' arrangement.

In np/pn cells, the fringing field has a lower absolute value and is mostly in plane, while the vertical component is weak and practically negligible at the center of the cell. P and E_{ff} are thus both parallel to the LN/N_F interface planes, and the required in-plane component of the field is present from the beginning due to the specific LN substrate arrangement. In these conditions, the polarization charges that cancel the internal field are generated at the N_F /air lateral interfaces and are most probably due to twist distortions compatible with P being parallel to the two bounding surfaces. Again, this creates an additional electric field that, in this case, is comparable in magnitude to the original value of the fringing field. The threshold charging that gives rise to the electromechanical instability is reached here at temperatures lower than those in the np/np cells, corresponding to higher values of P , and on average produce the ejection of a lower number of fluid jets. We understand this phenomenon to be a result of the weaker fringing field that characterizes this configuration. Noteworthy, experiments on N_F sessile droplets deposited on glass surfaces with patterned electrodes showed that jet ejection preferentially occurs in regions where the fringing field is in the vertical direction [26]. This is an additional indication that the in-plane electric field component, arising in these conditions due to the N_F superscreening, is higher than in any other configuration.

Once jets are formed in np/pn samples, they are, however, more disruptive compared to the other kind of cell. This is shown in Figure 2b, where the variation of the average droplet radius after each instability event is reported as a function of T_i . This parameter exhibits a decreasing trend for both configurations, but such a decreasing trend is different in the two situations, being smooth for the np/np cells and very steep for the np/pn ones.

In this latter case, the average radius decreases by more than 60% after the first instability events, indicating an extremely explosive and disruptive phenomenon.

We understand this behavior to be due to the radial shape of E_{eff} in the np/pn LN arrangement. Indeed, jets are polar fluid tubes carrying polarization charges on their tips, which thus keep on moving in the direction of the field, accelerated by the field itself. The polar nature of the ejected jets is well visualized in Figure 4a, where jets parallel to the polarizer appear dark, while those at 45 deg. exhibit the maximum brightness, showing that the liquid crystal director \mathbf{n} is along the jet axis. Since the polarization vector is locally collinear to the optical axis \mathbf{n} , Figure 4a indicates that \mathbf{P} is also along the jet's axis, in the direction of flow. Noteworthy, POM analysis of the nematic director in conditions involving thick cells with LN substrates is cumbersome and made difficult by the formation of a thick fluid bridge and by the birefringence of the substrates. For this reason, the image in Figure 4a is related to a RM734 N_F sessile droplet lying on a LN substrate. The results are, however, extendable to the double substrate configuration.

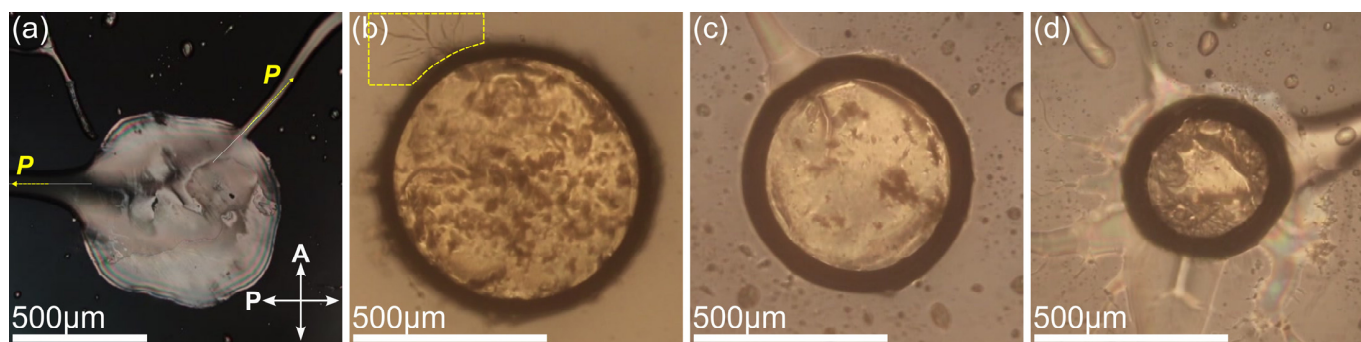


Figure 4. (a) RM734 N_F droplet on a LN substrate observed under a crossed polarizer. Jets parallel to either polarizer or analyzer appear dark, while those at 45 deg. exhibit the maximum brightness. This indicates that \mathbf{n} is along the jets' axis, which also defines the direction of the polarization vector \mathbf{P} . Note that the attribution of the specific direction of \mathbf{P} (parallel or antiparallel to \mathbf{n}) is here arbitrary; (b,c) evolution of the electromechanical instability of the N_F fluid bridge in case of a 150 μm thick np/pn cell. (b) Onset of the instability consisting in the formation of small spikes protruding from several portions of the bridge rim. The yellow dashed line identifies one very thin jet that branches on one of the bounding substrates; (c) as the instability proceeds, some of the small spikes retract or disrupt by forming tiny droplets, leaving only one large, main jet that continues to grow; (d) this is followed by the ejection of a large portion of the whole fluid mass from all around the bridge perimeter. Frames are not consecutive.

In the np/pn configuration, the in-plane field that accelerates the jet tips depends on the specific substrates' arrangement and remains approximately unperturbed during jet motion. On the contrary, in the np/np case, the in-plane component of the field is generated by N_F superscreening and depends on the position of the polarization charges. As such, it changes both value and direction as soon as jets protrude from the fluid bridge. In this case, there is not a "constant" radial field that moves the charged expelled fluid along a fixed direction, and jets do not show the collective disruptive motion observed in np/pn cells. The observed disruptive instability in np/pn cells might additionally be due to the acceleration experienced by the jets' tips, which may generate large distortions on the fluid bridge portions close to the ejection sites. This, in turn, causes additional charge accumulation in a sort of self-sustained effect.

An example of the instability of np/pn cells is reported in Figure 3e–h.

The evolution of the electromechanical instability of N_F fluid bridges is shown in more detail in Figure 4b–d. In these images, the gap between the LN crystals is larger than in Figure 3 (150 vs. 100 μm), which results in a more evident meniscus (thicker dark ring around the "droplet"). Figure 4b shows the appearance of small spikes that protrude from several portions of the bridge rim at the onset of the instability event. This is followed by

the formation of a single main jet (Figure 4c) and by the ejection of a large portion of the total fluid mass (Figure 4d). These events are accompanied by the decrease of the droplet diameter, which is quantified in Figure 2b for both kinds of cells. This specific sequence of frames is related to the *np/pn* configuration. Noteworthy, large variations of the droplet texture can be observed by comparing the three images, which suggests that instability induces severe rearrangements of the N_F liquid crystal polarization. This reasonably gives rise to the additional accumulation of bound charges which, in turn, stimulates additional fluid ejection as a strategy to decrease electrostatic energy.

Noteworthy, measuring the position of the jet tips from the initial frames after the ejection, we noticed that the average jet speed for equal values of T_i is higher in *np/pn* cells compared to the others, in agreement with the notion that fluid motion is faster in this configuration.

In conclusion, we studied the behavior of ferroelectric liquid bridges confined between two solid ferroelectric substrates arranged in different configurations realized so that, once pyroelectrically charged, they generate fringing fields of different values and shapes. Our observations highlighted that the features of the liquid crystal instability are affected by the specific fringing field profile in a way dominated by the minimization of the electrostatic energy associated with the bulk polarization of the ferroelectric fluid.

Our results show that the electromechanical instability of ferroelectric droplets confined between two ferroelectric solid substrates can be controlled in terms of instability, temperature, number of ejected jets and violence by acting on the substrates' arrangement. This might allow the realization of novel electro-hydrodynamic applications based on the electrostatic instability of polar liquids.

Author Contributions: Conceptualization, L.L.; methodology, L.L., S.M., R.Z. and R.B.; software, R.B.; validation, L.L. and S.M.; formal analysis, S.M. and A.S.O.; investigation, S.M.; data curation, S.M.; writing—original draft preparation, L.L. and R.Z.; writing—review and editing, L.L. and R.B.; supervision, L.L. and S.M. All authors have read and agreed to the published version of the manuscript.

Funding: L.L. and R.B. acknowledge the European Union—Next Generation EU, project code: ECS00000041; project title: Innovation, digitalization, and sustainability for the diffused economy in Central Italy—VITALITY.

Data Availability Statement: The raw data supporting the conclusions of this article will be made available by the authors on request.

Acknowledgments: L.L. and S.M. are thankful to Tommaso Bellini for useful discussions.

Conflicts of Interest: The authors declare no conflict of interest.

References

- Chen, X.; Korblova, E.; Dong, D.; Wei, X.; Shao, R.; Radzihovsky, L.; Glaser, M.A.; MacLennan, J.E.; Bedrov, D.; Walba, D.M.; et al. First-principles experimental demonstration of ferroelectricity in a thermotropic nematic liquid crystal: Polar domains and striking electro-optics. *Proc. Natl. Acad. Sci. USA* **2020**, *117*, 14021. [[CrossRef](#)] [[PubMed](#)]
- Mandle, R.J.; Cowling, S.J.; Goodby, J.W. A nematic-to-nematic transformation exhibited by a rod-like liquid crystal. *Phys. Chem. Chem. Phys.* **2017**, *19*, 11429–11435. [[CrossRef](#)] [[PubMed](#)]
- Nishikawa, H.; Shiroshita, K.; Higuchi, H.; Okumura, Y.; Haseba, Y.; Yamamoto, S.I.; Sago, K.; Kikuchi, H. A fluid liquid-crystal material with highly polar order. *Adv. Mater.* **2017**, *29*, 1702354. [[CrossRef](#)] [[PubMed](#)]
- Mandle, R.J.; Cowling, S.J.; Goodby, J.W. Rational design of rod-like liquid crystals exhibiting two nematic phases. *Chemistry* **2017**, *23*, 14554–14562. [[CrossRef](#)] [[PubMed](#)]
- Mertelj, A.; Cmok, L.; Sebastián, N.; Mandle, R.J.; Parker, R.R.; Whitwood, A.C.; Goodby, J.W.; Čopič, M. Splay nematic phase. *Phys. Rev. X* **2018**, *8*, 41025. [[CrossRef](#)]
- Lavrenovich, O.D. Ferroelectric nematic liquid crystal, a century in waiting. *Proc. Natl. Acad. Sci. USA* **2020**, *117*, 14629–14631. [[CrossRef](#)] [[PubMed](#)]
- Chen, X.; Korblova, E.; Glaser, M.A.; MacLennan, J.E.; Walba, D.M.; Clark, N.A. Polar in-plane surface orientation of a ferroelectric nematic liquid crystal: Polar monodomains and twisted state electro-optics. *Proc. Natl. Acad. Sci. USA* **2021**, *118*, e2104092118. [[CrossRef](#)] [[PubMed](#)]

8. Barboza, R.; Marni, S.; Ciciulla, F.; Mir, F.A.; Nava, G.; Caimi, F.; Zaltron, A.; Clark, N.A.; Bellini, T.; Lucchetti, L. Explosive electrostatic instability of ferroelectric liquid droplets on ferroelectric solid surfaces. *Proc. Natl. Acad. Sci. USA* **2022**, *119*, e2207858119. [[CrossRef](#)]
9. Sebastian, N.; Čopič, M.; Mertelj, A. Ferroelectric nematic liquid-crystalline phases. *Phys. Rev. E* **2022**, *106*, 021001. [[CrossRef](#)]
10. Zavvou, E.; Klasen-Memmer, M.; Manabe, A.; Bremer, M.; Eremin, A. Polarisation-driven magneto-optical and nonlinear-optical behaviour of a room-temperature ferroelectric nematic phase. *Soft Matter* **2022**, *18*, 8804. [[CrossRef](#)] [[PubMed](#)]
11. Máthé, M.T.; Perera, K.; Buka, Á.; Salamon, P.; Jákli, A. Fluid ferroelectric filaments. *Adv. Sci.* **2023**, *9*, 2305950. [[CrossRef](#)] [[PubMed](#)]
12. Marni, S.; Nava, G.; Barboza, R.; Bellini, T.; Lucchetti, L. Walking ferroelectric liquid droplets with light. *Adv. Mater.* **2023**, *35*, 2212067. [[CrossRef](#)] [[PubMed](#)]
13. Caimi, F.; Nava, G.; Fuschetto, S.; Lucchetti, L.; Paiè, P.; Osellame, R.; Chen, X.; Clark, N.A.; Glaser, M.A.; Bellini, T. Fluid superscreening and polarization following in confined ferroelectric nematics. *Nat. Phys.* **2023**, *19*, 1658–1666. [[CrossRef](#)]
14. Máthé, M.T.; Himel, M.S.H.; Adaka, A.; Gleeson, J.T.; Sprunt, S.; Salamon, P.; Jákli, A. Liquid Piezoelectric Materials: Linear Electromechanical Effect in Fluid Ferroelectric Nematic Liquid Crystals. *Adv. Funct. Mater.* **2024**, *34*, 2314158. [[CrossRef](#)]
15. Sebastián, N.; Lovšin, M.; Berteloot, B.; Osterman, N.; Petelin, A.; Mandl, R.J.; Aya, S.; Huang, M.; Drevenšek-Olenik, I.; Neyts, K.; et al. Polarization patterning in ferroelectric nematic liquids via flexoelectric coupling. *Nat. Commun.* **2023**, *14*, 3029. [[CrossRef](#)]
16. Basnet, B.; Rajabi, M.; Wang, H.; Kumari, P.; Thapa, K.; Paul, S.; Lavrentovich, M.O.; Lavrentovich, O.D. Soliton walls paired by polar surface interactions in a ferroelectric nematic liquid crystal. *Nat. Commun.* **2022**, *13*, 3932. [[CrossRef](#)] [[PubMed](#)]
17. Rayleigh, L. XX. On the equilibrium of liquid conducting masses charged with electricity. *Phil. Mag.* **1882**, *14*, 184–186. [[CrossRef](#)]
18. Habibpourmoghadam, A.; Lucchetti, L.; Evans, D.; Reshetnyak, V.; Omairat, F.; Schafforz, S.L.; Lorenz, A. Laser-induced erasable patterns in a N^* liquid crystal on an iron doped lithium niobate surface. *Opt. Express* **2017**, *25*, 26148. [[CrossRef](#)] [[PubMed](#)]
19. Carns, J.L.; Cook, G.; Saleh, M.A.; Serak, S.V.; Tabiryan, N.; Evans, D.R. Self-activated liquid-crystal cells with photovoltaic substrates. *Opt. Lett.* **2006**, *31*, 993. [[CrossRef](#)] [[PubMed](#)]
20. Sanna, S.; Schmidt, W.G. LiNbO₃ surfaces from a microscopic perspective. *J. Phys. Condens. Matter* **2017**, *29*, 413001. [[CrossRef](#)] [[PubMed](#)]
21. Kostritskii, S.M.; Sevostyanov, O.G.; Aillerie, M.; Bourson, P. Suppression of photorefractive damage with aid of steady-state temperature gradient in nominally pure LiNbO₃ crystals. *J. Appl. Phys.* **2008**, *104*, 114104. [[CrossRef](#)]
22. Kostritskii, S.M.; Aillerie, M.; Sevostyanov, O.G. Self-compensation of optical damage in reduced nominally pure LiNbO₃ crystals. *J. Appl. Phys.* **2010**, *107*, 123526. [[CrossRef](#)]
23. Ferraro, P.; Grilli, S.; Miccio, L.; Vespi, V. Wettability patterning of lithium niobate substrate by modulating pyroelectric effect to form microarray of sessile droplets. *Appl. Phys. Lett.* **2008**, *92*, 213107. [[CrossRef](#)]
24. Byer, R.L.; Roundy, C.B. Pyroelectric coefficient direct measurement technique and application to a nsec response time detector. *Ferroelectrics* **2011**, *43*, 333–338.
25. Gebre, T.; Batra, A.K.; Guggilla, P.; Aggarwal, M.D.; Lal, R.B. Pyroelectric properties of pure and doped lithium niobate crystals for infrared sensors. *Ferroelectr. Lett. Sect.* **2010**, *31*, 131–139. [[CrossRef](#)]
26. Máthé, M.T.; Farkas, B.; Péter, L.; Buka, Á.; Jákli, A.; Salamon, P. Electric field-induced interfacial instability in a ferroelectric nematic liquid crystal. *Sci. Rep.* **2023**, *13*, 6981. [[CrossRef](#)] [[PubMed](#)]
27. Rosensweig, R.E.; Zahn, M.; Shumovich, R.J. Labyrinthine instability in magnetic and dielectric fluids. *Magn. Magn. Mater.* **1983**, *39*, 127–132. [[CrossRef](#)]
28. Zahn, M.; Shumovich, R. Labyrinthine instability in dielectric fluids. *IEEE Trans. Ind. Appl.* **1985**, *21*, 53–61. [[CrossRef](#)]
29. Igonin, M.; Cebers, A. Labyrinthine instability of miscible magnetic fluids. *Phys. Fluids* **2003**, *15*, 1734. [[CrossRef](#)]

Disclaimer/Publisher's Note: The statements, opinions and data contained in all publications are solely those of the individual author(s) and contributor(s) and not of MDPI and/or the editor(s). MDPI and/or the editor(s) disclaim responsibility for any injury to people or property resulting from any ideas, methods, instructions or products referred to in the content.